

Spectroscopic and photometric studies of low-metallicity star-forming dwarf galaxies. II. HS 1442+4250

N. G. Guseva¹, P. Papaderos², Y. I. Izotov¹, R. F. Green³, K. J. Fricke², T. X. Thuan⁴, and K.G. Noeske²

¹ Main Astronomical Observatory, Ukrainian National Academy of Sciences, Zabolotnoho 27, Kyiv 03680, Ukraine

² Universitäts-Sternwarte, Geismarlandstraße 11, D-37083 Göttingen, Germany

³ National Optical Astronomy Observatory, Tucson, AZ 85726, USA

⁴ Astronomy Department, University of Virginia, Charlottesville, VA 22903, USA

Received ; Accepted

Abstract. We present broad-band V and I imaging and long-slit spectroscopy in the optical range $\lambda\lambda 3600 - 7500\text{\AA}$ of the dwarf irregular galaxy HS 1442+4250. The oxygen abundance $12 + \log(\text{O}/\text{H}) = 7.63 \pm 0.02$ ($Z = Z_{\odot}/19$)* in the brightest H II region of HS 1442+4250 places the galaxy among the most metal-deficient emission-line galaxies. The low metallicity and blue colour ($V - I$) ~ 0.4 mag of the low-surface-brightness (LSB) component make HS 1442+4250 a likely rare young dwarf galaxy candidate. We use four methods to estimate the stellar population age in the LSB component of HS 1442+4250. Different star formation histories are considered. The equivalent widths of hydrogen H α and H β emission lines, and of hydrogen H γ and H δ absorption lines, the spectral energy distribution and the observed ($V - I$) colours of the LSB regions are reproduced quite well by models with only young and intermediate-age stellar populations. By contrast, the observational data cannot be reproduced by a stellar population formed continuously with a constant star formation rate in the age range from 0 to $\gtrsim 2$ Gyr. While a faint old stellar population in HS 1442+4250 with an age $\gtrsim 2$ Gyr is not excluded, we find no evidence for such a population from the present data.

Key words. galaxies: abundances — galaxies: dwarf — galaxies: evolution — galaxies: compact — galaxies: starburst — galaxies: stellar content

1. Introduction

The dwarf irregular galaxy HS 1442+4250 (\equiv UGC 9497) from the Hamburg Survey (HS) was first classified as an emission-line galaxy by Sanduleak & Pesch (1982). With the coordinates $\alpha(\text{J2000.0}) = 14^{\text{h}}44^{\text{m}}12^{\text{s}}.1$, $\delta(\text{J2000.0}) = +42^{\circ}37'37''$ it is situated in the direction of a low-density region in the galaxy spatial distribution. HS 1442+4250 has been studied by Tift et al. (1986), Popescu et al. (1996), and Popescu & Hopp (2000) who were searching for dwarf galaxies in voids. Popescu & Hopp (2000) have measured the fluxes and equivalent widths of the emission lines in HS 1442+4250. They derived its redshift as $z = 0.0025$ and an oxygen abundance $12 + \log(\text{O}/\text{H}) = 7.89$. The galaxy has also been studied spectroscopically by Kniazev et al. (1998) and Pustilnik et al. (1999), who derived $12 + \log(\text{O}/\text{H}) = 7.68$ and 7.7 , respectively.

B and R surface photometry of HS 1442+4250 has been presented in Vennik et al. (1996). This galaxy with $M_B = -15.2$ mag was found to be one of the bluest dwarf

galaxies in their sample with $(B - R)_T = 0.42$ mag. This implies that the light from HS 1442+4250 is dominated by a relatively young stellar population.

In this paper we present V and I photometric and spectroscopic observations of HS 1442+4250. We study its properties and put constraints on the age of its low-surface-brightness (LSB) component. Throughout this paper we adopt a distance of 12.4 Mpc for the dwarf galaxy derived from its redshift $z = 0.0025$ and a Hubble constant of $75 \text{ km s}^{-1} \text{ Mpc}^{-1}$, after correction for Virgocentric infall (Kraan-Korteweg 1986). At this distance $1''$ corresponds to a linear size of 60 pc. The structure of the paper is as follows. In Sect. 2 we describe the observations and data reduction. The photometric properties of HS 1442+4250 are described in Sect. 3. In Sect. 4 we derive chemical abundances in its two brightest H II regions. The properties of its stellar populations are discussed in Sect. 5. Finally, Sect. 6 summarises our main conclusions.

Send offprint requests to: N.G. Guseva, guseva@mao.kiev.ua

* $12 + \log(\text{O}/\text{H})_{\odot} = 8.92$ (Anders & Grevesse 1989).

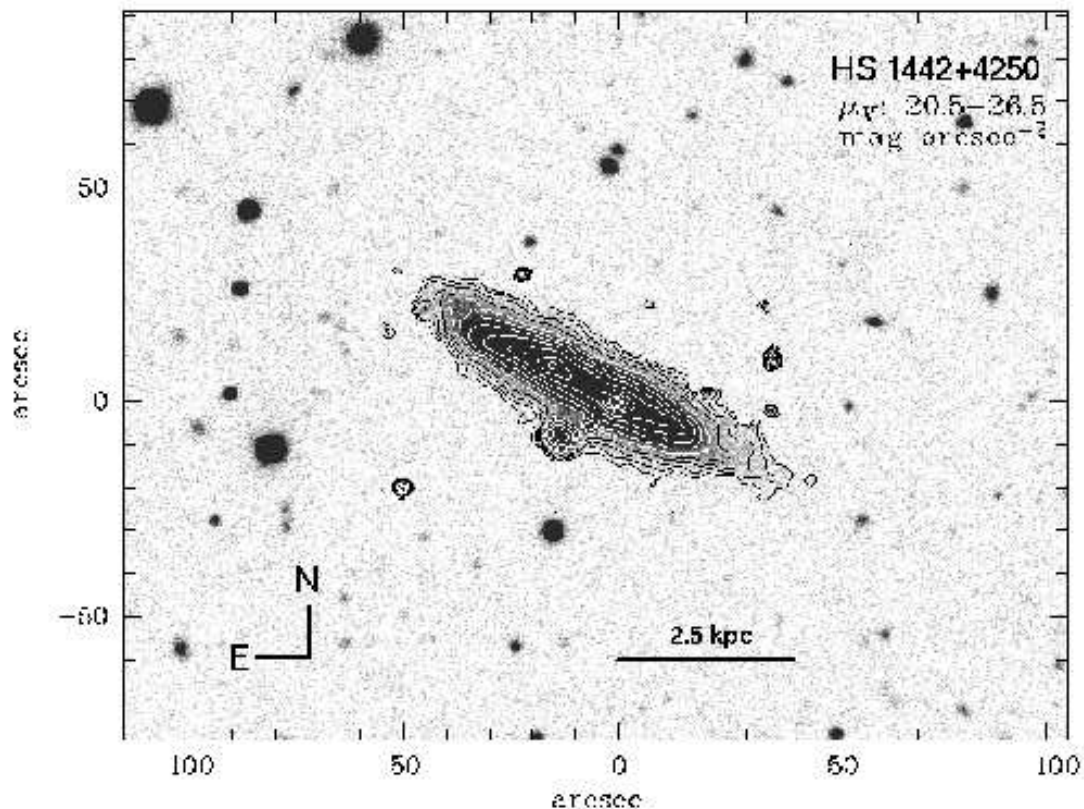


Fig. 1. V image of HS 1442+4250. The overlaid V contours correspond to surface brightness between 20.5 mag arcsec $^{-2}$ and 26.5 mag arcsec $^{-2}$ in steps of 0.5 mag.

2. Observations and data reduction

2.1. Photometric observations

Broad-band V and I images were obtained with the Kitt Peak 2.1m telescope¹ on April 18, 1999 during photometric conditions. The telescope was equipped with a thinned Tektronix 1024 \times 1024 CCD operating at a gain of $3\text{e}^- \text{ADU}^{-1}$ and giving an instrumental scale of $0''.305 \text{ pixel}^{-1}$ and a field of view of $5'$. The total exposures of 20 min in V and 40 min in I were split into three subexposures, slightly offset with respect to each other for removal of cosmic particle hits and bad pixels. The point spread function in V and I were respectively $1''.78$ and $1''.67$ FWHM.

Bias- and flat-field exposures were taken during the same night. The data reduction was done using IRAF². Images were calibrated by observing four different standard fields from Landolt (1992), each 3–4 times at different airmasses during the same night. Our calibration un-

certainties are estimated to be well below 0.05 mag in all bands. Reduction steps included bias subtraction, removal of cosmic particle hits, flat-field correction and absolute flux calibration.

2.2. Spectroscopic observations and data reduction

The spectroscopic observations of HS 1442+4250 were carried out on June 18, 1999, with the Kitt Peak 4m Mayall telescope, in combination with the Ritchey-Chrétien spectrograph and the T2KB 2048 \times 2048 CCD detector. The slit was centered on the brightest star-forming region and oriented along the elongated body of the galaxy with position angle P.A. = $60^\circ.4$, close to the direction of its major axis (see Fig. 1). The slit orientation during the observations was close to the parallactic angle to minimize the effects of differential refraction. Hence, no correction was made for this effect. A $2'' \times 300''$ slit with the KPC-10A grating in first order and a GG 375 order separation filter were used. The spatial scale along the slit was $0''.69 \text{ pixel}^{-1}$ and the spectral resolution $\sim 7 \text{ \AA}$ (FWHM). The spectra were obtained at an airmass of 1.44. The total exposure of 60 minutes was broken up into 3 subexposures. Two Kitt Peak spectrophotometric standard stars, Feige 34 and HZ 44, were observed for flux calibration. Spectra of a He-Ne-Ar comparison lamp were obtained for wavelength calibration.

¹ Kitt Peak National Observatory (KPNO) is operated by the Association of Universities for Research in Astronomy (AURA), Inc., under cooperative agreement with the National Science Foundation (NSF).

² IRAF is the Image Reduction and Analysis Facility distributed by the National Optical Astronomy Observatory, which is operated by the AURA under cooperative agreement with the NSF.

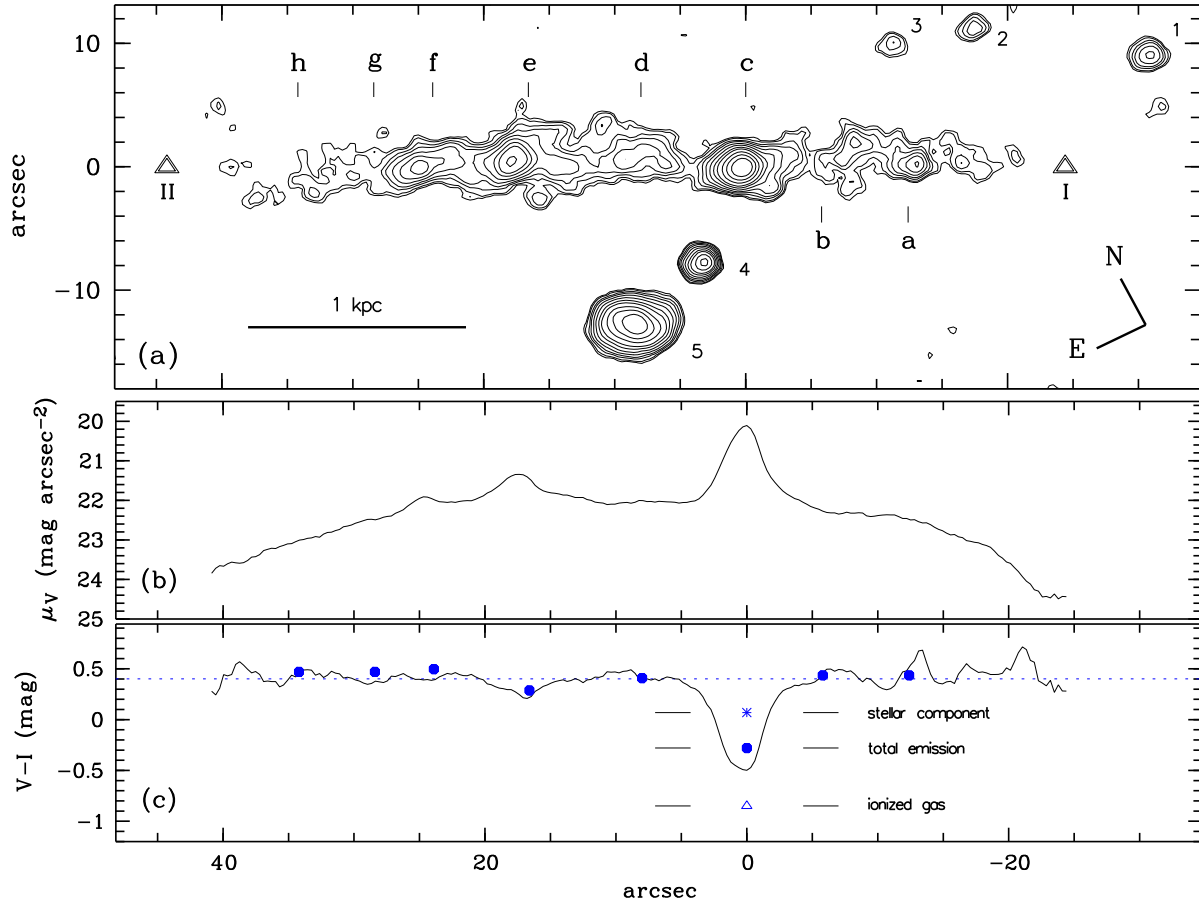


Fig. 2. (a) Contrast-enhanced *I* contour map of HS 1442+4250. The brighter regions labeled *c* and *e* and the fainter regions *a*, *b*, *d*, *f*, *g* and *h* are arranged along the major axis of the galaxy, over a projected length of $\sim 1'$ (3.5 kpc). Triangles, labeled I and II, show the positions of the outermost regions with $H\alpha$ and $H\beta$ emission and without any absorption features. Sources labeled 1 to 5 are significantly redder ($0.8 \leq (V - I) \lesssim 2.0$) than the LSB component ($(V - I) \sim 0.4$ mag) and most probably are not related to HS 1442+4250. (b) *V* surface brightness distribution along the major axis of HS 1442+4250 computed within a rectangular strip of $2''$ width. The origin is at the location of region *c*. The six compact regions indicated in the upper panel from *a* to *f* span a range in surface brightness between 20 and 22.6 *V* mag arcsec⁻² and regions *g* and *h* between 22.3 and 23 *V* mag arcsec⁻². (c) $(V - I)$ colour distribution within a $2''$ strip along the major axis of HS 1442+4250. The colour between regions *a* and *h* is nearly constant at ~ 0.4 mag (dotted line). The bluest region ($(V - I) \sim -0.5$ mag) is coincident with region *c*. Region *a* presents a large spatial colour variation and contains a compact source which is much fainter on the *V* image. This source has a maximal $(V - I)$ colour of 0.69 mag, being significantly redder than the adjacent regions (see also Fig. 3). Filled circles show the colours predicted for a stellar population formed continuously with a constant star formation rate in two periods with 1) intermediate-age and 2) young stellar population. The filled circle for region *c* indicates the colour of a 4 Myr stellar population to which has been added the observed ionized gas emission in region *c*. The asterisk shows the colour of a 4 Myr pure stellar population emission, while the open triangle shows the colour of ionized gas emission.

The data reduction was made with the IRAF software package. This includes bias subtraction, flat-field correction, cosmic-ray removal, wavelength calibration, night sky subtraction, correction for atmospheric extinction and absolute flux calibration of the two-dimensional spectra.

One-dimensional spectra for abundance determination in the two brightest H II regions *c* and *e* (Fig. 2a, 3) were extracted within apertures of $2'' \times 2''.8$.

In addition we extracted one-dimensional spectra of six regions in the LSB component of the galaxy showing

hydrogen Balmer absorption lines. The selected regions, labeled in Fig. 2a *a*, *b*, *d*, *f*, *g* and *h*, are listed in Tables 4 and 5 together with their positions relative to the brightest region *c* and their angular extent along the slit. We also extracted one-dimensional spectra of two additional outermost regions labeled I and II with only $H\alpha$ and $H\beta$ emission.

3. Imaging

3.1. Morphology

Photometric signatures of a young to moderately evolved stellar population are present all along the major axis of HS 1442+4250. The $(V - I)$ colour map (Fig. 3) shows that the bluest region coincides with the brightest region c (Fig. 2) where $(V - I) \sim -0.5$ mag. This region is partly resolved and has an effective radius of $2''.4$ (≈ 140 pc) and a mean FWHM of $2''.5$ in V . Its apparent V magnitude of 18.0 mag corresponds to an absolute V magnitude of ~ -12.5 mag. The $(V - I)$ colour of the second brightest region e ($V = 19.65$ mag) is ~ 0.2 mag, markedly bluer than the local LSB component with an average $(V - I)$ colour of ~ 0.4 mag. Sources c and e contribute more than 80% of the flux in excess of the LSB component inside the 25 V mag arcsec $^{-2}$ isophote. Several other fainter compact sources are seen along the major axis of the galaxy (Fig. 2a). Variations of the $(V - I)$ colour on spatial scales of $2'' - 3''$ (Fig. 3) imply that non-uniform extinction may be significant. Alternatively, it may be that part of the reddest small regions are due to background/foreground red sources. This is likely to be the case for the compact region a , clearly detected in both the I image and the colour map, but marginally seen in V . Roughly $15''$ SE of region c there is a red, relatively bright ($V = 18.6$ mag) source labeled 5 with a mean $(V - I) \gtrsim 1.2$ mag, i.e., roughly 0.6 mag redder than the LSB component of HS 1442+4250 (see Fig. 4b). The surface brightness profile of this source can be fitted by a Sérsic profile (Sérsic 1968) with a V central surface brightness of ≈ 21.9 mag arcsec $^{-2}$ and an exponent η of ~ 0.7 (see Eq. 1 in Guseva et al. 2003). Most likely, this source as well as those labeled 1 – 4 in Fig. 2a are background galaxies.

3.2. Surface brightness and colour distribution

The surface brightness profiles (SBPs) of HS 1442+4250 in Fig. 4a were obtained using one of the methods (method iii) described in Papaderos et al. (1996a) and Guseva et al. (2003) after the red compact sources 1 through 5 in Fig. 2a have been fitted and subtracted from the combined V and I images. The extended sources 4 and 5 overlap with the LSB component of HS 1442+4250 at a surface brightness fainter than 24.5 V mag arcsec $^{-2}$. In this case, a two-dimensional model was fitted to their light distribution and subtracted from the original images. To ensure that possible residuals in the subtraction of sources 4 and 5 do not affect the surface photometry, SBPs were computed by fitting ellipses to isophotes after screening out the area subtended by position angles $-145^\circ \leq \phi \leq -95^\circ$ with respect to region c .

The SBPs of HS 1442+4250 (Fig. 4a) are well fitted by an exponential in the radius range $15'' \lesssim R^* \lesssim 26''$, corresponding to a surface brightness fainter than ~ 24 V mag arcsec $^{-2}$. In this range we obtain a V band scale

length of $\approx 4''.5$, in good agreement with the value of $4''.2$ derived previously in the B band by Vennik et al. (2000).

However, an inward extrapolation of the exponential fit predicts for radii between $5''$ and $10''$ a higher intensity than that observed (not shown in Fig. 4a). Therefore an exponential model flattening for small radii appears to be necessary to adequately fit the LSB emission of HS 1442+4250. This conclusion is in line with the results by Vennik et al. (2000) who noted the convex shape of the SBP of HS 1442+4250 over a substantial radius range. Indeed, for radii $\geq 15''$, by fitting a Sérsic (1968) profile to the SBPs in Fig. 4 we obtain an exponent η of ~ 1.2 and 1.3 in V and I , respectively, slightly greater than that corresponding to a pure exponential distribution ($\eta = 1$).

Alternatively, a fitting formula which reproduces an inward flattening of the exponential distribution has been discussed by Papaderos et al. (1996a, their Eq. 22; see also Guseva et al. 2003 for a detailed explanation). Near the center, such an intensity distribution depends on the relative central intensity depression $q = \Delta I/I_0$, where I_0 is the central intensity obtained by extrapolation of the outer exponential slope to $R^* = 0$, and on the cutoff-radius $b\alpha$ inside of which the central flattening occurs.

We find that fits to the SBPs for radii $R^* \geq 15''$ adopting a Sérsic law are nearly indistinguishable from those given by Eq. 22 of Papaderos et al. (1996a) with $b = 2.1$ and $q = 0.3$ (Fig. 4a). Both fits predict a central surface brightness of ~ 21.8 V mag arcsec $^{-2}$ for the LSB component (Fig. 4a), which is roughly 1.3 mag fainter than the value $\mu_{E,0}$ predicted by extrapolation of the exponential fit from the outer SBP part to $R^* = 0$. The surface brightness distribution of the residual emission in excess of the LSB model (Fig. 4a, crosses) is to be attributed to star-forming regions along the major axis of HS 1442+4250 (starburst component). The integrated V magnitudes inside the 25 and 27 V mag arcsec $^{-2}$ isophotes are 17.65 and 17.35 mag, respectively. Such values imply that the starburst component contributes $\lesssim 20\%$ and 10% of the HS 1442+4250 total light in the V inside the respective isophotal radii. About one half of the total starburst component emission originates from region c (Fig. 2a, 3).

Table 1 summarizes the derived photometric quantities. They are not corrected for inclination and foreground Galactic extinction. Cols. 2 and 3 give, respectively, the central surface brightness $\mu_{E,0}$ and scale length α of the LSB component obtained from exponential fits to the SBPs for $R^* \geq 15''$ and weighted by the photometric uncertainty of each point. For the apparent major-to-minor axis ratio of 4.1 at 26.5 V mag arcsec $^{-2}$ and assuming a disk geometry for the LSB component the inclination-corrected central surface brightness is ~ 1.2 mag fainter than the value quoted in col.2. In columns 4 and 5 we show the apparent magnitudes m_{LSB} of a pure exponential distribution ($q = 0$) and m_{LSB}^c of an inwards flattening distribution (Eq.22 in Papaderos et al. 1996a) with the derived flattening parameters $(b, q) = (2.1, 0.3)$. Note that both distributions refer to the same extrapolated central surface brightness $\mu_{E,0}$ and α (cols. 2 and 3). Columns 6

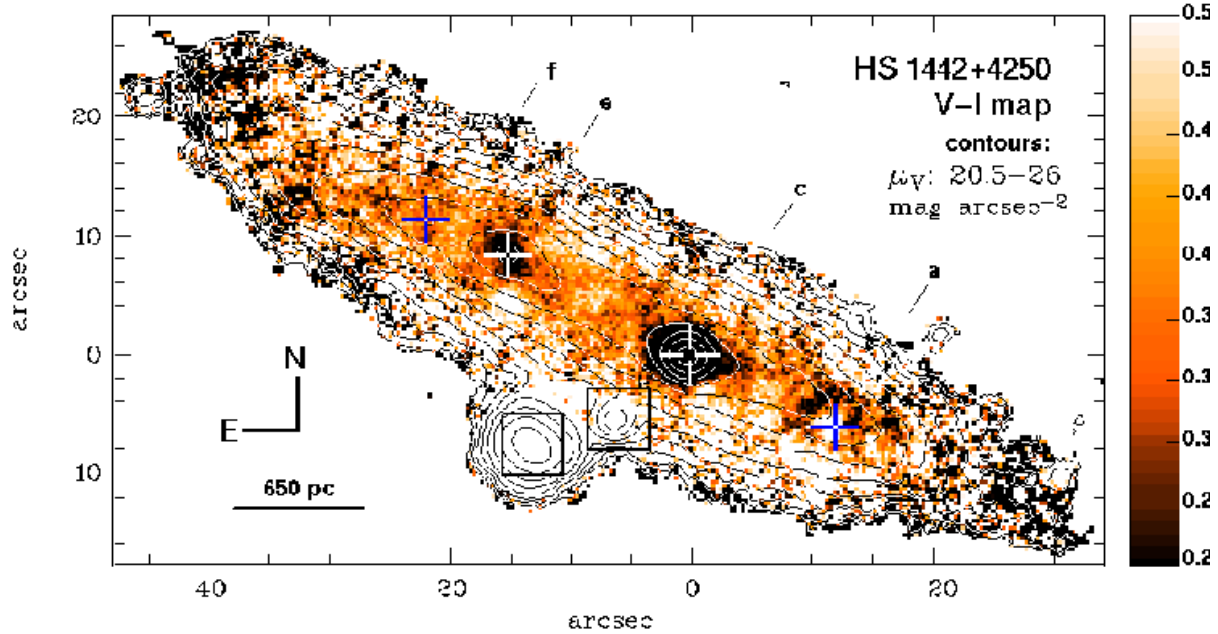


Fig. 3. $(V - I)$ colour map of HS 1442+4250 displayed in the range 0.25 to 0.55 mag. The colours are corrected for foreground Galactic extinction ($A_V = 0.044$ mag, $A_I = 0.026$ mag). The overlaid contours are from 20.5 to 26 V mag arcsec $^{-2}$ in steps of 0.5 mag. Crosses along the major axis of the galaxy mark the positions of regions *a*, *f* (black crosses) and *c*, *e* (white crosses) (see Fig. 2a). The positions of the red sources 4 and 5 are marked by squares. The bluest region with $(V - I) \sim -0.5$ mag coincides with region *c*.

Table 1. Structural properties of the starburst and LSB components.

Band	$\mu_{E,0}$ mag arcsec $^{-2}$	α pc	m_{LSB} mag	m_{LSB}^c mag	P_{25} pc	$m_{P_{25}}$ mag	E_{25} pc	$m_{E_{25}}$ mag	m_{SBP} mag	m_{tot} mag	r_{eff}, r_{80} pc
(1)	(2)	(3)	(4)	(5)	(6)	(7)	(8)	(9)	(10)	(11)	(12)
<i>V</i>	20.50 ± 0.08	272 ± 6	15.23	15.54	496	17.65	1127	15.65	15.37 ± 0.02	15.35	503,822
<i>I</i>	20.18 ± 0.20	291 ± 15	14.76	15.07	709	17.31	1290	15.16	14.95 ± 0.03	14.93	556,880

through 9 list quantities obtained from profile decomposition whereby the intensity distribution of the LSB component was modeled by the modified exponential distribution proposed by Papaderos et al. (1996a). In cols. 6 and 8 we tabulate the radial extents P_{25} and E_{25} of the starburst and LSB components respectively, both determined at a surface brightness 25 mag arcsec $^{-2}$ (see Fig. 4b). The respective apparent magnitudes of each component within P_{25} and E_{25} are listed in cols. 7 and 9. The total magnitude of HS 1442+4250 derived from SBP integration out to the outermost radius of $\approx 26''$ is listed in col. 10. The apparent magnitude of the galaxy, obtained within a polygonal aperture after removal of sources 1 through 5 (Fig. 2a) is given in col. 11. In col. 12 we list the effective radius r_{eff} and the radius r_{80} which encircles 80% of the galaxy's total flux.

As shown in Fig. 4b, the $(V - I)$ colour of HS 1442+4250 beyond the radius P_{25} increases with an average gradient of 0.24 mag kpc $^{-1}$. The observed gradual colour increase is in agreement with the linear slope derived by subtracting the modeled distributions for the LSB component (thick-gray lines in Fig. 4b). From the colour profile we derive a mean $(V - I) = 0.63 \pm 0.05$ mag in the

radius range $15'' \leq R^* \leq 26''$. The $(V - I)$ colour at $R^* \geq 18''$ is uncertain, and it is not clear whether the colour gradient is attributable to HS 1442+4250, or caused by the background sources and residuals after their subtraction.

4. Chemical abundances

In this Section we analyze the element abundances in the two brightest H II regions *c* and *e*. Their spectra, shown in Fig. 5, are characterised by strong nebular emission lines.

The emission line fluxes were measured by Gaussian profile fitting. The errors of the line fluxes include the errors in the fitting of profiles and those in the placement of the continuum. They have been propagated in the calculations of the elemental abundance errors. The spectra were corrected for interstellar extinction with the extinction coefficient $C(\text{H}\beta)$ derived from the hydrogen Balmer decrement using the equations from Izotov et al. (1994) and the theoretical hydrogen emission line flux ratios from Brocklehurst (1971). The emission line fluxes relative to the $\text{H}\beta$ emission line flux, both observed ($F(\lambda)$) and corrected for extinction and underlying stellar hydrogen absorption ($I(\lambda)$), the equivalent widths EW of the emission

lines, the observed fluxes of the $H\beta$ emission line, and the equivalent widths of the hydrogen absorption lines for regions c and e are listed in Table 2.

Our measured fluxes of the emission lines in region c are in fair agreement with those from Popescu & Hopp (2000) except for the $[O\text{ II}]\lambda 3727\text{\AA}$ emission line which in our case is ~ 2 times weaker. The agreement between our measured emission line fluxes and those by Kniazev et al. (1998) and Pustilnik et al. (1999) is much better.

Note that the flux of the $\text{He II } \lambda 4686$ nebular emission line in region c is relatively high ($\sim 3\%$ of the $H\beta$ flux) (Table 2) implying that hard radiation beyond $\lambda 228\text{\AA}$ is intense. Such a property is not unusual for hot supergiant $H\text{ II}$ regions in low-metallicity dwarf galaxies. Strong $\text{He II } \lambda 4686$ nebular emission has also been detected in I Zw 18 ($Z_{\odot}/50$, e.g., Izotov et al. 1999), SBS 0335–052 ($Z_{\odot}/40$, Izotov et al. 1997, 1999), Tol 1214–277 ($Z_{\odot}/23$, e.g., Fricke et al. 2001), SBS 1415+437 ($Z_{\odot}/21$, Thuan et al. 1995, 1999) and some other low-metallicity galaxies (Guseva et al. 2000).

Only a few strongest emission lines are detected in the spectra of the two outermost regions I and II. The observed fluxes and EW s of the $H\alpha$ and $H\beta$ emission lines in these regions are listed in Table 4. Since the continuum in the red part of the spectra in those regions is weak, the $EW(H\alpha)$ are very uncertain. The extinction coefficient $C(H\beta)$ for regions I and II is set to 0.

The photoionization model used to convert line fluxes into abundances is the same as described in Guseva et al. (2003). The ionic and heavy element abundances for regions c and e together with electron temperatures, electron number densities and adopted ICFs are given in Table 3.

4.1. Heavy element abundances

The oxygen abundances in regions c and e are $12 + \log(O/H) = 7.63 \pm 0.02$ ($Z \sim Z_{\odot}/19$) and 7.54 ± 0.20 ($Z \sim Z_{\odot}/24$), respectively. These two determinations agree within the errors. However, the oxygen abundance in region e may have been underestimated. This is because the weak $[O\text{ III}]\lambda 4363$ emission line [$I(\lambda 4363)/I(H\beta) = 0.055$ (Table 2)] may be enhanced by shocks. This effect is likely lower in region c where the $[O\text{ III}]\lambda 4363$ emission line is stronger. For comparison, Popescu & Hopp (2000) obtained for HS 1442+4250 $12 + \log(O/H) = 7.89$, while Kniazev et al. (1998) and Pustilnik et al. (1999) derived $12 + \log(O/H) = 7.68$ and 7.7 , respectively. The former value is significantly larger than ours due to the higher $[O\text{ II}]\lambda 3727\text{\AA}$ and lower $[O\text{ III}]\lambda 4363\text{\AA}$ fluxes measured by Popescu & Hopp (2000).

The neon-to-oxygen abundance ratio $\log \text{Ne}/O = -0.75$ for region c is in good agreement with the mean ratio derived from previous studies of BCDs (e.g., Izotov & Thuan 1999). The nitrogen-to-oxygen abundance ratio $\log N/O = -1.44$ is ~ 0.15 dex higher than the N/O ratios obtained by Thuan et al. (1995) and Izotov & Thuan (1999) for the very metal-deficient BCDs with $Z \lesssim Z_{\odot}/20$.

Table 3. Element abundances in regions c and e .

Value	region c	region e
$T_e(\text{O III})(\text{K})$	17810 ± 320	16410 ± 4100
$T_e(\text{O II})(\text{K})$	14960 ± 250	14390 ± 3420
$T_e(\text{S III})(\text{K})$	16480 ± 260	15320 ± 3400
$N_e(\text{S II})(\text{cm}^{-3})$	10 ± 10	10 ± 10
$O^+/H^+(\times 10^5)$	0.467 ± 0.022	1.372 ± 0.890
$O^{+2}/H^+(\times 10^5)$	3.685 ± 0.159	2.067 ± 1.279
$O^{+3}/H^+(\times 10^6)$	1.464 ± 0.194	...
$O/H(\times 10^5)$	4.299 ± 0.188	3.439 ± 1.558
$12 + \log(O/H)$	7.63 ± 0.02	7.54 ± 0.20
$N^+/H^+(\times 10^7)$	1.702 ± 0.128	5.361 ± 2.585
ICF(N) ^a	9.20	2.51
$\log(N/O)$	-1.438 ± 0.038	-1.408 ± 0.287
$\text{Ne}^{+2}/H^+(\times 10^5)$	0.662 ± 0.035	0.467 ± 0.300
ICF(Ne) ^a	1.17	1.66
$\log(\text{Ne}/O)$	-0.746 ± 0.030	-0.646 ± 0.342
$S^+/H^+(\times 10^7)$	0.700 ± 0.036	...
$S^{+2}/H^+(\times 10^7)$	5.593 ± 0.725	...
ICF(S) ^a	2.30	...
$\log(S/O)$	-1.473 ± 0.054	...
$\text{Ar}^{+2}/H^+(\times 10^7)$	1.185 ± 0.070	...
$\text{Ar}^{+3}/H^+(\times 10^7)$	1.420 ± 0.252	...
ICF(Ar) ^a	1.01	...
$\log(\text{Ar}/O)$	-2.213 ± 0.048	...
$\text{He}^+/H^+(\lambda 4471)$	0.075 ± 0.007	...
$\text{He}^+/H^+(\lambda 5876)$	0.078 ± 0.003	...
$\text{He}^+/H^+(\lambda 6678)$	0.077 ± 0.006	...
$\text{He}^+/H^+(\text{mean})$	0.078 ± 0.002	...
$\text{He}^{+2}/H^+(\lambda 4686)$	0.003 ± 0.000	...
$\text{He}/H(\lambda 4471)$	0.078 ± 0.007	...
$\text{He}/H(\lambda 5876)$	0.081 ± 0.003	...
$\text{He}/H(\lambda 6678)$	0.080 ± 0.006	...
$\text{He}/H(\text{mean})$	0.080 ± 0.002	...
$Y(\lambda 4471)$	0.237 ± 0.022	...
$Y(\lambda 5876)$	0.244 ± 0.009	...
$Y(\lambda 6678)$	0.242 ± 0.018	...
$Y(\text{mean})$	0.243 ± 0.008	...

^aICF is the ionization correction factor.

4.2. He abundances

The He I emission lines in region c are strong, allowing a reliable determination of the He abundance. Five $\text{He I } \lambda 3889, \lambda 4471, \lambda 5876, \lambda 6678, \lambda 7065$ emission lines are used to correct their fluxes self-consistently for collisional and fluorescent enhancement (see the method description in Izotov et al. 1994). Then the He^+ abundance is derived from the corrected $\text{He I } \lambda 4471, \lambda 5876, \lambda 6678$ emission line fluxes. Some fraction of He ($\sim 3.8\%$) is in the He^{+2} form as derived from the $\text{He II } \lambda 4686$ emission line flux. The total helium abundance is derived as the sum of the He^+ and He^{+2} abundances and is shown in Table 3 for each of the three He I lines used for the abundance determination.

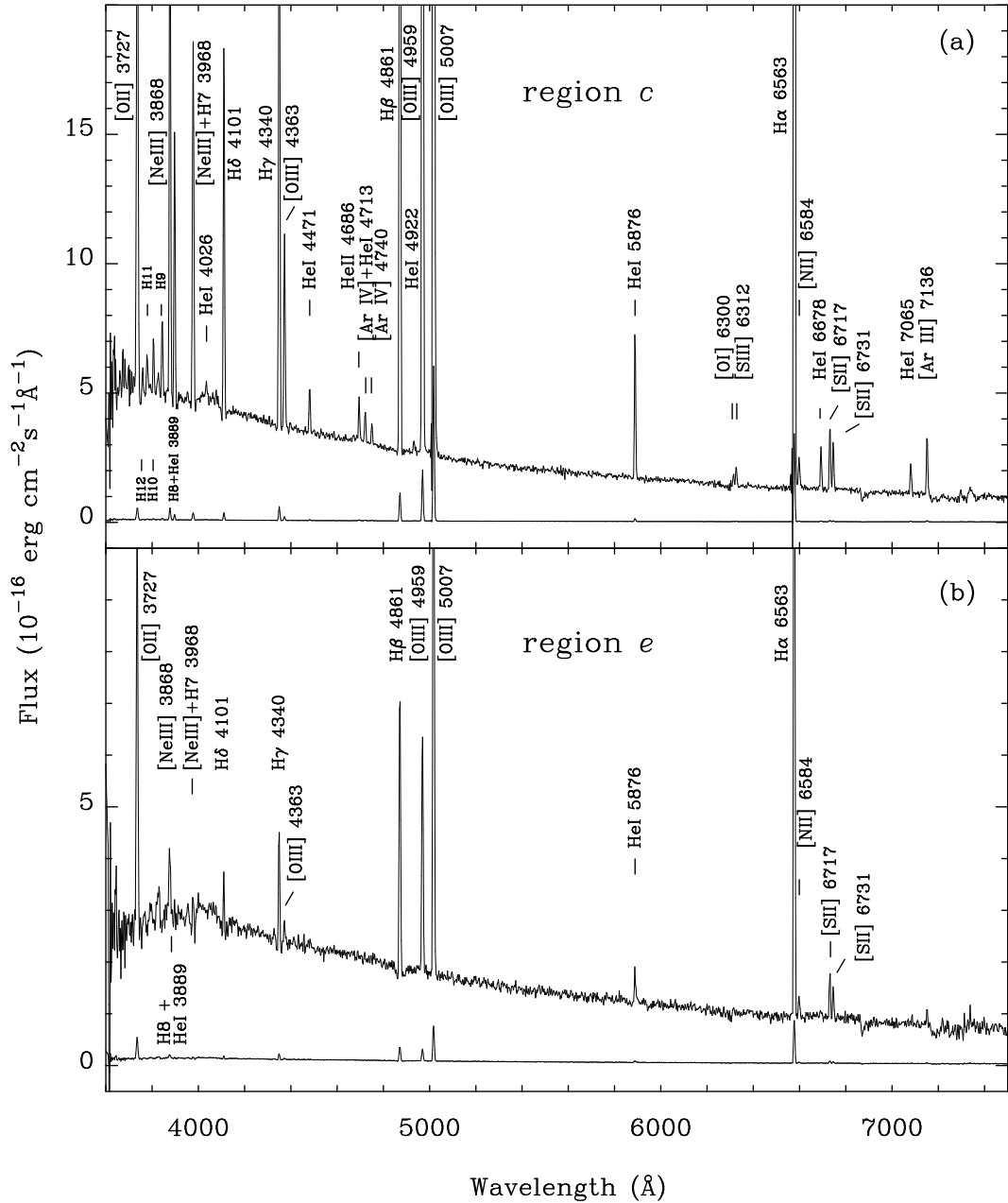


Fig. 5. The spectra of regions *c* and *e*. The lower spectra in (a) and (b) are the observed spectra downsampled by factors of 50 and 20, respectively.

The mean value of the He mass fraction $Y = 0.243 \pm 0.008$ obtained for region *c* (see Table 3), is consistent with the primordial ^4He mass fraction $Y_p = 0.244 \pm 0.002$, derived by extrapolating the Y vs O/H linear regression to $\text{O}/\text{H} = 0$ (Izotov & Thuan 1998), and with $Y_p = 0.245 \pm 0.002$ derived for the two most metal-deficient BCDs, known, I Zw 18 and SBS 0335–052 (Izotov et al. 1999). However, the He abundance in region *c* is likely slightly underestimated because of underlying stellar He I absorption. Due to the relatively small equivalent widths of the He I emission lines (Table 2) the effect of the underlying absorption may lead to an underestimate of the He^+ abundance by 1% – 2% in the case of the strongest He I $\lambda 5876$ line. This effect is larger for the weaker He I $\lambda 4471$ and $\lambda 6678$ emission

lines. In region *e* only weak He I $\lambda 3889$ and $\lambda 5876$ emission lines are observed. Therefore, an accurate He abundance determination is not possible in that region.

5. The stellar populations

The low metallicity of HS 1442+4250 suggests that it may be a young nearby dwarf galaxy (Izotov & Thuan 1999). However, the morphological properties of the galaxy, such as the presence of multiple star-forming regions on the one hand, and a redder extended diffuse stellar component on the other hand, suggest that stars in HS 1442+4250 have been formed during several episodes of star formation. We study in this section the properties of the stellar popu-

Table 2. Observed ($F(\lambda)$) and corrected ($I(\lambda)$) fluxes and equivalent widths (EW) of emission lines in regions c and e .

$\lambda_0(\text{\AA})$ Ion	region c			region e		
	$F(\lambda)/F(\text{H}\beta)$	$I(\lambda)/I(\text{H}\beta)$	$EW(\text{\AA})$	$F(\lambda)/F(\text{H}\beta)$	$I(\lambda)/I(\text{H}\beta)$	$EW(\text{\AA})$
3727 [O II]	0.496 \pm 0.008	0.535 \pm 0.009	38.3 \pm 0.8	1.477 \pm 0.089	1.376 \pm 0.094	24.4 \pm 1.8
3750 H12	0.020 \pm 0.004	0.027 \pm 0.006	1.6 \pm 0.4
3771 H11	0.028 \pm 0.004	0.035 \pm 0.006	2.1 \pm 0.4
3798 H10	0.034 \pm 0.003	0.042 \pm 0.006	2.6 \pm 0.4
3835 H9	0.056 \pm 0.004	0.065 \pm 0.006	4.4 \pm 0.4
3868 [Ne III]	0.405 \pm 0.007	0.432 \pm 0.008	32.1 \pm 0.7	0.260 \pm 0.048	0.242 \pm 0.048	4.0 \pm 1.4
3889 H8 + He I	0.176 \pm 0.005	0.193 \pm 0.007	15.0 \pm 0.6	0.070 \pm 0.033	0.171 \pm 0.089	1.2 \pm 1.0
3968 [Ne III] + H7	0.280 \pm 0.006	0.302 \pm 0.007	24.1 \pm 0.7	0.144 \pm 0.034	0.237 \pm 0.078	2.5 \pm 1.0
4026 He I	0.015 \pm 0.004	0.016 \pm 0.004	2.0 \pm 0.5
4101 H δ	0.260 \pm 0.006	0.277 \pm 0.007	24.9 \pm 0.7	0.174 \pm 0.032	0.261 \pm 0.065	3.1 \pm 1.0
4340 H γ	0.467 \pm 0.008	0.486 \pm 0.008	50.0 \pm 1.0	0.374 \pm 0.039	0.438 \pm 0.056	7.4 \pm 1.4
4363 [O III]	0.134 \pm 0.004	0.138 \pm 0.004	14.2 \pm 0.7	0.058 \pm 0.028	0.055 \pm 0.028	1.3 \pm 1.2
4388 He I	0.005 \pm 0.002	0.005 \pm 0.002	0.6 \pm 0.4
4471 He I	0.034 \pm 0.003	0.035 \pm 0.003	3.8 \pm 0.5
4686 He II	0.030 \pm 0.003	0.030 \pm 0.003	3.7 \pm 0.6
4713 [Ar IV] + He I	0.022 \pm 0.003	0.022 \pm 0.003	2.7 \pm 0.6
4740 [Ar IV]	0.014 \pm 0.002	0.014 \pm 0.002	1.8 \pm 0.5
4861 H β	1.000 \pm 0.012	1.000 \pm 0.012	147.1 \pm 1.9	1.000 \pm 0.063	1.000 \pm 0.070	25.7 \pm 2.5
4922 He I	0.010 \pm 0.003	0.010 \pm 0.003	1.4 \pm 0.6
4959 [O III]	1.769 \pm 0.019	1.754 \pm 0.018	250.0 \pm 2.6	0.831 \pm 0.057	0.774 \pm 0.057	20.1 \pm 2.4
5007 [O III]	5.032 \pm 0.046	4.976 \pm 0.046	782.3 \pm 4.3	2.489 \pm 0.130	2.317 \pm 0.130	62.5 \pm 6.9
5876 He I	0.099 \pm 0.003	0.094 \pm 0.003	22.7 \pm 1.3	0.100 \pm 0.026	0.093 \pm 0.026	3.6 \pm 2.0
6300 [O I]	0.009 \pm 0.002	0.008 \pm 0.002	2.4 \pm 0.8
6312 [S III]	0.016 \pm 0.002	0.014 \pm 0.002	4.4 \pm 0.9
6563 H α	3.012 \pm 0.028	2.763 \pm 0.029	881.8 \pm 6.8	2.900 \pm 0.147	2.738 \pm 0.162	133.8 \pm 6.9
6584 [N II]	0.025 \pm 0.002	0.023 \pm 0.002	7.5 \pm 1.0	0.070 \pm 0.019	0.066 \pm 0.019	3.3 \pm 2.0
6678 He I	0.028 \pm 0.002	0.026 \pm 0.002	8.6 \pm 1.1
6717 [S II]	0.046 \pm 0.002	0.042 \pm 0.002	13.9 \pm 1.2	0.147 \pm 0.024	0.137 \pm 0.025	7.0 \pm 2.5
6731 [S II]	0.032 \pm 0.002	0.029 \pm 0.002	9.7 \pm 1.1	0.095 \pm 0.020	0.088 \pm 0.020	4.6 \pm 2.1
7065 He I	0.023 \pm 0.002	0.020 \pm 0.002	7.8 \pm 1.1
7136 [Ar III]	0.043 \pm 0.002	0.038 \pm 0.002	15.8 \pm 1.4
$C(\text{H}\beta)$ dex		0.110 \pm 0.013			0.000 \pm 0.063	
$F(\text{H}\beta)^a$		3.85 \pm 0.03			0.44 \pm 0.02	
$EW(\text{abs})$ \AA		0.4 \pm 0.4			1.45 \pm 1.0	

^ain units 10^{-14} erg s $^{-1}$ cm $^{-2}$.

lations in the extended LSB component and discuss the evolutionary status of HS 1442+4250.

For this we use four different methods, three of them based on the spectroscopic data and the fourth one using photometric data. Two of these methods are based on the time evolution of equivalent widths of hydrogen Balmer line emission and absorption which are detected in almost all regions along the slit. The other two methods are based on the comparison of observed with theoretical spectral energy distributions (SED) and broad-band colours. All the aforementioned methods are sensitive to the star formation history. The first two methods are extinction-insensitive, while the others depend on both the properties of the stellar population and the interstellar extinction. The use of all four methods allows us to put constraints on the star formation history and properties of the stellar population as well as to estimate the interstellar extinc-

tion. These methods are described in detail in Guseva et al. (2001, 2003).

The observed ($V - I$) colour of the brightest region c is very blue ~ -0.5 (Fig. 2c), and cannot be reproduced by a stellar population of any age. This is because of the large contribution of very strong oxygen and hydrogen emission lines, as evidenced by their large equivalent widths (Table 2), and gaseous continuum. Gaseous emission is also an important contributor to the total light of regions I and II. However, in other regions the equivalent widths of the emission lines are small (Table 4). Therefore, for those regions we will not take into account ionized gas emission.

5.1. Age from Balmer nebular emission lines

The equivalent widths of hydrogen nebular emission lines are usually used as an age indicator of star-forming regions, in which O and early B stars are still present. The

equivalent widths of these lines for an instantaneous burst decrease sharply after ~ 10 Myr (e.g., Schaerer & Vacca 1998). However, in the case of continuous star formation this method can be successfully used for age determination in the 0 – 10 Gyr range (Guseva et al. 2001).

For the age determination we use the two brightest hydrogen emission lines, $H\alpha$ and $H\beta$. Their fluxes and equivalent widths, measured in the spectra of the extracted LSB regions are shown with errors in Table 4.

Because the $H\beta$ emission line is narrower than the absorption line in these regions and does not fill the absorption component, its flux was measured using the continuum level at the bottom of the absorption line. This level has been chosen by visually interpolating from the absorption line wings to the center of the line.

The extinction coefficients $C(H\beta)$ in regions with detectable $H\alpha$ and $H\beta$ emission lines are derived from the observed $H\alpha/H\beta$ flux ratios. The theoretical recombination $H\alpha/H\beta$ flux ratio of 2.8 is adopted, which is typical for low-metallicity H II regions. No correction for the absorption line equivalent widths has been made. The extinction coefficients $C(H\beta)$ are shown in Table 4. Note, that $C(H\beta)$ for region f is uncertain because of the low equivalent width of the $H\beta$ emission line which is comparable to the equivalent width of the absorption line.

The dependence of the $H\alpha$ and $H\beta$ emission line equivalent widths on age for a heavy element mass fraction $Z_{\odot}/20$ has been calculated for two limiting star formation histories, the case of an instantaneous burst, and that of a continuous constant star formation. The calculations are done with the galactic evolution code PEGASE.2 (Fioc & Rocca-Volmerange 1997). The time evolution of $H\alpha$ in the case of an instantaneous burst is shown in Fig. 6a by a thick solid line. We next consider the case of continuous star formation with a constant star formation rate (SFR). The temporal evolution of the equivalent widths of the $H\beta$ and $H\alpha$ emission lines is calculated using the model equivalent widths of hydrogen emission lines and SEDs for an instantaneous burst (Fioc & Rocca-Volmerange 1997). The temporal dependences of the $H\alpha$ emission line equivalent width are shown in Fig. 6a by different thin lines for continuous star formation starting at time t_i , as defined by the abscissa value, and stopping at t_f (the curves in Fig. 6a are labeled by $\log t_f$). Time is zero now and increases to the past.

To compare theoretical predictions with observed data we consider in the following regions a and f only, as representative of the whole LSB component. The positions of the measured $EW(H\alpha)$ on the model curve for continuous star formation with $t_f = 8$ Myr are shown in Fig. 6a by a triangle for region a and by a star for region f . In this case the data are consistent with star formation starting not earlier than $t_i \sim 20$ Myr ago for region a and ~ 200 Myr ago for region f . If instead continuous star formation stopping at $t_f = 0$ is considered, then the observed $EW(H\beta)$ and $EW(H\alpha)$ are consistent with models in which star formation starts at time $t_i \sim 1 - 4$ Gyr ago for region a and $t_i \gg 10$ Gyr ago for region f . Hence, we conclude that for

region f , models in which stars are continuously forming until now ($t_f = 0$) with a constant star formation rate are inconsistent with the observed $EW(H\alpha)$ and $EW(H\beta)$.

5.2. Age from Balmer stellar absorption lines

Hydrogen Balmer absorption lines are detected along the slit in a large part of HS 1442+4250. This allows us to estimate the age of stellar populations by comparing the observed hydrogen absorption line equivalent widths with theoretical ones. González Delgado et al. (1999) have calculated the temporal dependence of the Balmer absorption lines considering both instantaneous and continuous star formation. Their models for an instantaneous burst predict a steady increase of the equivalent widths with time for ages ranging from 1 Myr to 1 Gyr, reaching maximum values $EW(H\gamma) \sim 12\text{\AA}$ and $EW(H\delta) \sim 15\text{\AA}$ for a metallicity $Z = Z_{\odot}/20$ (Fig. 6b). For solar metallicity, the predicted maximum EW s are larger by $\sim 1\text{\AA}$. However, González Delgado et al. (1999) do not extend calculations to ages > 1 Gyr, when the equivalent widths of the absorption lines decrease with age (Bica & Alloin 1986a).

We compared the model predictions of the $H\delta$ absorption line equivalent width for an instantaneous burst by González Delgado et al. (1999) (Fig. 9 in Guseva et al. 2003) with the empirical calibration by Bica & Alloin (1986a) (Fig. 6b) and with available observational data for a large sample of different objects: open and globular stellar clusters (Bica & Alloin 1986a, 1986b), nuclei of normal elliptical and spiral galaxies (Bica & Alloin 1987; Bica 1988; Schmidt et al. 1989, 1995; Saraiva et al. 2001) with different ages and metallicities. No stellar clusters and galaxies with $EW(H\gamma) > 9.6\text{\AA}$ and $EW(H\delta) > 12\text{\AA}$ were found in the samples considered. Hence, the models by González Delgado et al. (1999) at ages ~ 1 Gyr apparently overestimate the equivalent widths of the absorption lines.

Therefore we only use an empirical calibration of Balmer absorption line equivalent widths versus age by Bica & Alloin (1986a) for ages ranging between 1 Myr and 16.5 Gyr. This calibration is based on integrated spectra of 63 star clusters with known ages, metallicities and reddenings. Later, a calibration of the $H\gamma$ and $H\delta$ absorption line equivalent widths was derived by Schmidt et al. (1995) to apply to starburst events in dwarf galaxies. The dependence of the equivalent width of the $H\delta$ absorption line on age for an instantaneous burst from the data of Bica & Alloin (1986a) is shown in Fig. 6b by thick solid line.

We also consider the case of continuous star formation. For this we assume that stars are forming with a constant star formation rate starting at time t_i and stopping at t_f . We use the equivalent widths of hydrogen absorption lines from the empirical calibration by Bica & Alloin (1986a) and SEDs by Fioc & Rocca-Volmerange (1997) for instantaneous bursts to calculate the temporal evolution of the

Table 4. Fluxes, equivalent widths of H α and H β emission lines and the extinction coefficient $C(\text{H}\beta)$ in LSB regions.

Region	Distance ^a	Aperture ^b	$F(\text{H}\alpha)^c$	$EW(\text{H}\alpha)^d$	$F(\text{H}\beta)^c$	$EW(\text{H}\beta)^d$	$C(\text{H}\beta)$
I	-24.4	2.0 \times 4.1	8.0 \pm 0.5	1200.0 \pm 2.5	3.0 \pm 0.5	32.8 \pm 0.8	0.0
<i>a</i>	-12.4	2.0 \times 7.6	50.4 \pm 0.6	78.9 \pm 1.8	17.9 \pm 0.5	14.6 \pm 0.7	0.00 \pm 0.07
<i>b</i>	-5.8	2.0 \times 4.1	22.0 \pm 0.6	36.5 \pm 0.8	7.2 \pm 0.6	7.3 \pm 0.5	0.12 \pm 0.07
<i>d</i>	8.0	2.0 \times 5.5	53.9 \pm 0.3	52.4 \pm 2.5	17.1 \pm 0.6	9.9 \pm 0.5	0.15 \pm 0.07
<i>f</i>	23.9	2.0 \times 4.1	13.6 \pm 0.6	16.8 \pm 1.8	2.8 \pm 0.5	3.1 \pm 0.7	0.31 \pm 0.07
<i>g</i>	28.4	2.0 \times 4.8	17.4 \pm 0.6	31.7 \pm 0.8
<i>h</i>	34.2	2.0 \times 6.9	5.5 \pm 0.3	12.4 \pm 1.9
II	44.2	2.0 \times 6.2	13.2 \pm 0.3	634.4 \pm 2.5	4.9 \pm 0.6	32.4 \pm 0.5	0.0

^adistance from region *c* in arcsec. Negative and positive values correspond to regions located respectively to the southwest and northeast from region *c*.

^baperture $x \times y$ where x is the slit width and y the size along the slit in arcsec.

^cin units $10^{-16} \text{ erg s}^{-1} \text{ cm}^{-2}$.

^din Å.

Table 5. Equivalent widths of H γ and H δ absorption lines in LSB regions.

Region	Distance ^a	Aperture ^b	$EW(\text{H}\delta)^{c,d}$	$EW(\text{H}\gamma)^{c,d}$	$EW(\text{H}\delta)_{B\&A}^{c,e}$	$EW(\text{H}\gamma)_{B\&A}^{c,e}$
<i>a</i>	-12.4	2.0 \times 7.6	9.0 \pm 0.6	...	9.8 \pm 0.6	...
<i>b</i>	-5.8	2.0 \times 4.1	8.6 \pm 0.4	6.6 \pm 0.5	8.9 \pm 0.4	6.7 \pm 0.4
<i>d</i>	8.0	2.0 \times 5.5	7.3 \pm 0.5	5.3 \pm 0.5	7.8 \pm 0.5	5.0 \pm 0.5
<i>f</i>	23.9	2.0 \times 4.1	6.2 \pm 0.7	5.1 \pm 0.9	6.6 \pm 0.7	5.1 \pm 0.7
<i>g</i>	28.4	2.0 \times 4.8	7.2 \pm 0.4	4.8 \pm 0.9	7.8 \pm 0.4	5.1 \pm 0.4
<i>h</i>	34.2	2.0 \times 6.9	7.4 \pm 0.5	5.3 \pm 0.5	7.6 \pm 0.5	7.4 \pm 0.5

^adistance from region *c* in arcsec. Negative and positive values correspond to regions located respectively to southwest and northeast from region *c*.

^baperture $x \times y$ where x is the slit width and y the size along the slit in arcsec.

^cin Å.

^dequivalent widths are measured using Gaussian fitting of the lines.

^eequivalent widths are obtained within the same wavelength intervals $\lambda_0 = 4318 - 4364\text{Å}$ and $4082 - 4124\text{Å}$, respectively, for H γ and H δ as those used by Bica & Alloin (1986a).

equivalent widths of hydrogen absorption lines for continuous star formation.

The results are given in Fig. 6b. The temporal dependences of the equivalent width of the H δ absorption line are shown by different thin lines for continuous star formation starting at t_i , as defined by the abscissa value, and stopping at t_f (the curves in Fig. 6b are labeled by $\log t_f$). The equivalent width of the H δ absorption line in the spectrum of the stellar population formed between t_i and t_f corresponds in Fig. 6b to the EW at time t_i .

Stellar hydrogen absorption lines have been detected in all LSB regions. In all regions except for region *a*, we measure the equivalent widths of the H δ and H γ absorption lines. The H γ absorption line in region *a* has not been used because of the strong contamination by nebular emission. The contribution of the nebular H γ and H δ emission lines to the corresponding absorption lines in the spectra of regions *a*, *b*, *d*, *f*, *g* and *h* has been removed using the IRAF software package. For the northeastern regions *f*, *g*, and *h*, the contamination of the H δ and H γ absorption lines by nebular emission is small, resulting in a correction which is within the errors of the EW s.

Table 5 lists the equivalent widths with errors of the H γ and H δ absorption lines. The equivalent widths shown

in cols. (4) and (5) are measured using Gaussian fitting of the lines, while the EW s in cols. (6) and (7) marked with the subscript “B&A” are obtained within the same wavelength intervals $\lambda_0 = 4318 - 4364\text{Å}$ and $4082 - 4124\text{Å}$, respectively, for H γ and H δ as those used by Bica & Alloin (1986a).

The positions of the observed $EW(\text{H}\delta)$ on the model curve for continuous star formation with $t_f = 8$ Myr are shown in Fig. 6b by triangles for region *a* and by a star for region *f*. The observed $EW(\text{H}\delta)$ and $EW(\text{H}\gamma)$ are consistent with those of stellar populations forming continuously from ~ 40 –250 Myr ago to 8 Myr ago if the model calculations by González Delgado et al. (1999) are used. These models are shown in Fig. 9 of Guseva et al. (2003). In the case of the empirical calibration by Bica & Alloin (1986a) the observed $EW(\text{H}\delta)$ (Fig. 6b) and $EW(\text{H}\gamma)$ are best reproduced by a stellar population forming continuously with a constant star formation rate starting at $t_i \sim 50$ Myr for region *f* and ~ 1 Gyr for region *a* and stopping at $t_f = 8$ Myr.

Comparison of Figs. 6a and 6b shows that the ages of the oldest stars contributing to the light of region *f* (stars) derived from the emission and absorption line equivalent widths are consistent and lie in the narrow interval be-

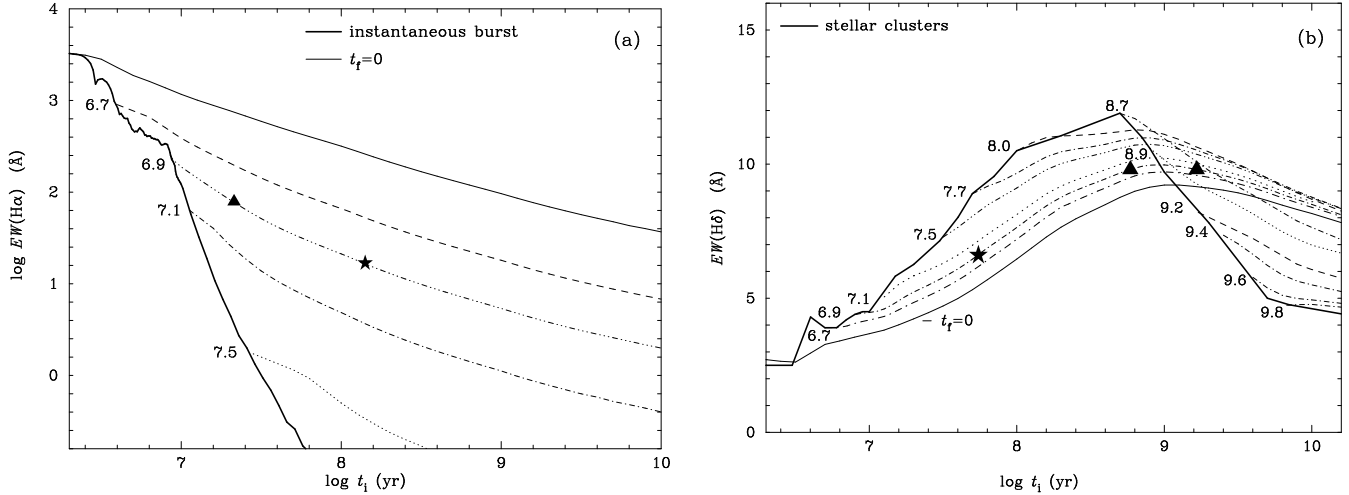


Fig. 6. (a) Temporal evolution of the equivalent width of the $H\alpha$ emission line for an instantaneous burst (thick solid line) and a heavy element mass fraction $Z = Z_{\odot}/20$ calculated with the PEGASE.2 code (Fioc & Rocca-Volmerange 1997). Other different lines show model predictions for continuous star formation with constant SFR, starting at the time t_i ago, defined by the abscissa, and stopping at t_f , with $t_f = 0$ (thin solid line) and t_f changing from 5 Myr to 30 Myr ago. Each line is labeled by the respective $\log t_f$ (t_f in yr). The positions of the observed $EW(H\alpha)$ on the modeled curve are shown for region *a* by triangle and for region *f* by star for the case of continuous star formation with $t_f = 8$ Myr. (b) Equivalent width of the $H\delta$ absorption line vs age for stellar clusters (Bica & Alloin 1986a) (thick solid line). The predicted $EW(H\delta)$ are also shown for continuous star formation with constant SFR starting at time t_i ago, defined by the abscissa, and stopping at t_f , with $t_f = 0$ (thin solid line) and t_f from 5 Myr to 6.3 Gyr. Each line is labeled by the respective $\log t_f$ (t_f in yr). The positions of the observed $EW(H\delta)$ on the modeled curve for region *a* are shown by triangles and the position of the observed $EW(H\delta)$ for region *f* is shown by star for the case of continuous star formation with $t_f = 8$ Myr. The equivalent widths have been measured in the same wavelength intervals as those used by Bica & Alloin (1986a).

tween 50 – 150 Myr. This implies that continuous star formation stopping at $t_f = 8$ Myr is a reasonable scenario for region *f*. However, the ages of the stellar population in region *a* derived from Figs. 6a and 6b (triangles) are not in agreement. The age of the oldest stars contributing to the light of this region as derived from the emission lines is ~ 25 Myr, while the age derived from the absorption lines using the González Delgado et al. (1999) and Bica & Alloin (1986a) calibrations is ~ 300 Myr and $\sim 1 - 2$ Gyr, respectively. Evidently, continuous star formation stopping at $t_f = 8$ Myr does not reproduce the observed properties of region *a*. A better agreement is achieved if star formation in this region continues until now (i.e. $t_f = 0$, thin solid lines in Fig. 6a and 6b). Then, within the errors, the observed data gives ages ~ 500 Myr (using González Delgado et al., 1999) and ~ 1 Gyr (Fig. 6b) for the oldest stars, which is in better agreement with the age estimation $\sim 2 - 3$ Gyr obtained from the equivalent widths of emission lines. Note, that choosing $t_f = 0$ is a limiting case which gives a maximum age of the old stellar population in a scenario with a constant star formation rate.

5.3. Age from the spectral energy distribution

We next consider the age of the stellar population derived from the comparison of the observed and theoretical SEDs. The shape of the observed spectrum reflects not only the properties of the stellar population but also reddening effects. Therefore only a combination of the SED method with those discussed in Sect. 5.1 and 5.2 allows us to simultaneously estimate age and interstellar extinction for the LSB regions in HS 1442+4250.

To fit the observed SEDs, we use the galactic evolution code PEGASE.2 (Fioc & Rocca-Volmerange 1997) to produce a grid of theoretical SEDs for an instantaneous burst of star formation with ages ranging between 0 and 10 Gyr, and a heavy element mass fraction $Z = Z_{\odot}/20$. An initial mass function with a Salpeter slope ($\alpha = -2.35$), and upper and lower mass limits of $120 M_{\odot}$ and $0.1 M_{\odot}$ are adopted. The contribution of gaseous emission to the total emission of regions *a*, *b*, *d*, *f*, *g* and *h* is small and has not been taken into account in the SED calculations.

A reliable determination of reddening can only be made for the two brightest H II regions *c* and *e* because of their many strong hydrogen emission lines (Table 2). In other regions, only $H\alpha$ and $H\beta$ emission lines are present. The latter line is very weak in regions *f*, *g* and *h*. The

extinction coefficient $C(H\beta)$ obtained from the Balmer decrement in the different regions ranges from 0 to 0.15. $C(H\beta)$ is 0.11 in the brightest region c .

We consider only the properties of region f , taken to be representative of the LSB region. We showed in Sect. 5.1 and 5.2 that the observed equivalent widths of the hydrogen emission and absorption lines in this region can be reproduced by a stellar population formed continuously with a constant SFR, starting at $t_i \sim 100$ Myr and stopping at $t_f = 8$ Myr. However, the observed SED of region f cannot be reproduced by a synthetic SED with such a young stellar population (lower spectra in Fig 7a) without assuming a non-negligible reddening. In particular, the observed SED can be fitted by a synthetic SED of a stellar population formed continuously between 10 and 50 Myr with a constant SFR, if there is an extinction $C(H\beta) = 0.29$ (upper spectra in Fig. 7a).

Alternatively, the observed SED of region f at $\lambda \gtrsim 3900\text{\AA}$ can also be well fitted by a synthetic SED of a stellar population formed continuously between 0 and 10 Gyr, if the SFR during the last 50 Myr was enhanced by a factor b of 10 and no reddening is present (SED labeled “b=10” in Fig. 7b). However, the fit is not satisfactory at shorter wavelengths. Additionally, this model does not reproduce the observed $EW(H\alpha)$ and $EW(H\beta)$.

We also consider models with star formation occurring in two episodes separated by a quiescent period. A model with star formation occurring with a constant SFR during (1) 1 – 10 Gyr and (2) 10 – 50 Myr with comparable masses of stellar populations formed in each period (not shown in Fig. 7) is able to reproduce the observed EW s of the hydrogen lines ($EW(H\alpha) = 11\text{\AA}$, $EW(H\beta) = 2\text{\AA}$, $EW(H\gamma) = -5.7\text{\AA}$ and $EW(H\delta) = -6.7\text{\AA}$). However, in that case the observed SED is again not well fitted at $\lambda < 3900\text{\AA}$. All the observational data for region f are best fitted by a model in which the stellar population formed continuously with a constant SFR in two periods 1) 0.5 – 2 Gyr and 2) 8 – 30 Myr ago and no reddening is present (Fig. 7c). If some extinction is present then ages will be smaller.

In summary, we conclude that only young and intermediate-age stellar populations can reproduce the observed properties of region f .

5.4. Age from the colour distribution

We derived V and I surface brightness and colour distributions for the regions covered by the spectroscopic observations and compared them with predictions from our population synthesis modeling. The results of this comparison are shown in Fig. 2c. The predicted colours obtained from convolving the theoretical SEDs with the appropriate filter bandpasses are shown by different symbols. The transmission curves for the Johnson V and Cousins I bands are taken from Bessell (1990). The zero points are from Bessell et al. (1998).

The contribution of the gaseous emission to the total brightness is small in the LSB component. Therefore, we do not take it into account. The colours of regions a and b are well fitted by those of a stellar population formed continuously with a constant SFR in two periods of star formation: (1) 100 – 400 Myr and (2) 4 – 15 Myr ago. The colours of the northeastern part of the galaxy excluding the brightest region c are best fitted by those of a stellar population forming continuously with a constant SFR in two periods: (1) 0.5 – 2 Gyr and (2) 8 – 30 Myr ago. In all cases we adopt $C(H\beta)=0$, which gives upper limits to the ages.

Since the contribution of ionized gas emission to the total light of the brightest H II region (region c) is high, the theoretical SED for this region has been constructed using a 4 Myr stellar population SED for a heavy element mass fraction $Z = Z_\odot/20$, and adding the gaseous continuum SED and observed emission lines (see Guseva et al. 2001 for details). The predicted $(V - I)$ colour of region c is reddened adopting $C(H\beta) = 0.11$ (Table 2). The observed colour $(V - I) \sim -0.5$ mag of this region is bluer than that of a 4 Myr stellar population (labeled by an asterisk in Fig. 2c) implying a large contribution of ionized gas emission (labeled by a triangle in Fig. 2c).

In Fig. 2c we show with filled circles the modeled colours of all regions in the LSB component of the galaxy and the total colour of region c . The agreement between the observed and synthetic $(V - I)$ colours is very good. The reddest colours $(V - I) \sim 0.63$ mag in HS 1442+4250 are found in the outer parts of the galaxy at $\mu_V \geq 24$ mag arcsec $^{-2}$ (Fig. 4). No spectroscopic data are available for these regions. Therefore, we can only use photometric data to estimate the age of the stellar population in those regions. Again, the maximum age depends on the adopted star formation history. If an instantaneous burst model is assumed then the age of the population with $(V - I) = 0.63$ mag is ~ 1 Gyr. In the case of continuous star formation the same colour can be explained by a stellar population formed with a constant star formation rate between 0 and 5 Gyr. We note, however, that the age estimates for the outer part of HS 1442+4250 are uncertain due to large errors in the $(V - I)$ colour and likely contamination of the LSB light by red background/foreground objects.

6. Conclusions

We present a detailed photometric and spectroscopic study of the low-metallicity dwarf irregular galaxy HS 1442+4250. Broad-band V and I images and spectra in the optical range have been obtained with the 2.1m and 4m Kitt Peak telescopes respectively. The main conclusions of this study can be summarized as follows:

1. HS 1442+4250 is a low-metallicity nearby ($D = 12.4$ Mpc) dwarf irregular galaxy with a chain of H II regions arranged along an elongated low-surface-brightness (LSB) component. The LSB component is well fitted by an exponential profile with a scale length

- $\alpha \gtrsim 270$ pc in its outer part, flattening for small radii ($R^* \lesssim 2\alpha$). The observed ($V - I$) colour of the brightest H II region is very blue ~ -0.5 mag due to the combined effect of a young stellar population and ionized gas emission. The colour of the LSB component is constant and equal to ~ 0.4 mag in a large part of the galaxy.
- The oxygen abundance for the brightest H II region c is $12 + \log(\text{O}/\text{H}) = 7.63$ ($Z = Z_{\odot}/19$). The neon-to-oxygen abundance ratio for this region, $\log \text{Ne}/\text{O} = -0.75$, is in good agreement with the mean ratio derived from previous studies of dwarf galaxies (e.g., Izotov & Thuan 1999). The nitrogen-to-oxygen abundance ratio $\log \text{N}/\text{O} = -1.44$ is ~ 0.15 dex larger than the N/O ratios obtained by Thuan et al. (1995) and Izotov & Thuan (1999) for the most metal-deficient blue compact dwarf (BCD) galaxies with $Z \lesssim Z_{\odot}/20$.
 - The ^4He mass fraction $Y = 0.243 \pm 0.008$ derived for the brightest H II region is in good agreement with the primordial ^4He mass fraction $Y_p = 0.244 - 0.245$ derived by Izotov & Thuan (1998) and Izotov et al. (1999).
 - We use four methods to estimate the age of the stellar population in the LSB component of HS 1442+4250. Different histories of star formation are considered. The spectroscopic data such as the equivalent widths of the hydrogen $\text{H}\alpha$ and $\text{H}\beta$ emission lines, and of the hydrogen $\text{H}\gamma$ and $\text{H}\delta$ absorption lines, the spectral energy distributions and the photometric colours are reproduced quite well by models with only young and intermediate-age stellar populations. It is unlikely that a significant old stellar population contributes much to the observed light in the inner regions. However, in the outermost regions of the LSB component, with $(V - I) \sim 0.63$, the presence of older populations is not excluded. For these regions only photometric data are available. The observed colour can be explained by a stellar population continuously forming between 0 and 5 Gyr with a constant SFR. However, because of large photometric errors and possible confusion with background sources, those age estimates are uncertain.
- Acknowledgements.** N.G.G. and Y.I.I. acknowledge DFG grant 436 UKR 17/2/02 and Y.I.I. is grateful for the Gauss professorship of the Göttingen Academy of Sciences. They are also grateful for Swiss SCOPE 7UKPJ62178 grant and for hospitality at Göttingen Observatory. Y.I.I. and T.X.T. acknowledge partial financial support through NSF grant AST-02-05785. Research by P.P. and K.J.F. has been supported by the Deutsches Zentrum für Luft- und Raumfahrt e.V. (DLR) under grant 50 OR 9907 7. K.G.N. thanks support from the Deutsche Forschungsgemeinschaft (DFG) grants FR 325/50-1 and FR 325/50-2.
- ## References
- Anders, E., & Grevesse, N. 1989, *Geochim.Cosmochim.Acta*, 53, 197
- Bessell, M. S. 1990, *PASP*, 102, 1181
- Bessell, M. S., Castelli, F., & Plez, B. 1998, *A&A*, 333, 231
- Bica, E. 1988, *A&A*, 195, 76
- Bica, E., & Alloin, D. 1986a, *A&AS*, 66, 171
- Bica, E., & Alloin, D. 1986b, *A&A*, 162, 21
- Bica, E., & Alloin, D. 1987, *A&AS*, 70, 281
- Binggeli, B., & Cameron, L. M. 1991, *A&A*, 252, 27
- Brocklehurst, M. 1971, *MNRAS*, 153, 471
- Caon, N., Capaccioli, M., & D’Onofrio, M. 1993, *MNRAS*, 265, 1013
- Fioc, M., & Rocca-Volmerange, B. 1997, *A&A*, 326, 950
- Fricke, K. J., Izotov, Y. I., Papaderos, P., Guseva, N. G., & Thuan, T. X. 2001, *AJ*, 121, 169
- Garnett, D. R. 1992, *AJ*, 103, 1330
- González Delgado, R. M., Leitherer, C., & Heckman, T. M. 1999, *ApJS*, 125, 489
- Guseva, N. G., Izotov, Y. I., & Thuan, T. X. 2000, *ApJ*, 531, 776
- Guseva, N. G., Izotov, Y. I., Papaderos, P., et al. 2001, *A&A*, 378, 756
- Guseva, N. G., Papaderos, P., Izotov, Y. I., et al. 2003, *A&A*, in press
- Izotov, Y. I., & Thuan, T. X. 1998, *ApJ*, 500, 188
- Izotov, Y. I., & Thuan, T. X. 1999, *ApJ*, 511, 639
- Izotov, Y. I., Thuan, T. X., & Lipovetsky, V. A. 1994, *ApJ*, 435, 647
- Izotov, Y. I., Lipovetsky, V. A., Chaffee, F. H., et al. 1997, *ApJ*, 476, 698
- Izotov, Y. I., Chaffee, F. H., Foltz, C. B., et al. 1999, *ApJ*, 527, 757
- Kniazev, A. Y., Pustilnik, S. A., & Ugryumov, A. V. 1998, *Bulletin Spec. Astrophys. Obs.*, 46, 23
- Kraan-Korteweg, R. C. 1986, *A&AS*, 66, 255
- Landolt, A. U. 1992, *AJ*, 104, 340
- Makarova, L. 1999, *A&A*, 139, 491
- Papaderos, P., Loose, H.-H., Thuan, T. X., & Fricke, K. J. 1996a, *A&AS*, 120, 207
- Papaderos, P., Loose, H.-H., Fricke, K. J., & Thuan, T. X. 1996b, *A&A*, 314, 59
- Popescu, C. C., & Hopp, U. 2000, *A&AS*, 142, 247
- Popescu, C. C., Hopp, U., Hagen, H. J., & Elsässer, H. 1996, *A&AS*, 116, 43
- Pustilnik, S. A., Engels, D., Ugryumov, A. V., et al. 1999, *A&AS*, 137, 299
- Sanduleak, N., & Pesch, P. 1982, *ApJ*, 258, L11
- Saraiva, M. F., Bica, E., Pastoriza, M. G., & Bonatto, C. 2001, *A&A*, 376, 43
- Schaerer, D., & Vacca, W. D. 1998, *ApJ*, 497, 618
- Schmidt, A. A., Alloin, D., & Bica, E. 1995, *MNRAS*, 273, 945
- Schmidt, A. A., Bica, E., & Dottori, H. A. 1989, *MNRAS*, 238, 925
- Sérsic, J. L. 1968, *Atlas de Galaxias Australes* (Córdoba: Obs. Astron.)
- Stasińska, G. 1990, *A&AS*, 83, 501
- Thuan, T. X., Izotov, Y. I., & Lipovetsky, V. A. 1995, *ApJ*, 445, 108
- Thuan, T. X., Izotov, Y. I., & Foltz, C. B. 1999, *ApJ*, 525, 105
- Tift, W. G., Kirshner, R. P., Gregory, S. A., & Moody, J. W. 1986, *ApJ*, 310, 75
- Vennik, J., Hopp, U., Kovachev, B., et al. 1996, *A&AS*, 117, 216
- Vennik, J., Hopp, U., & Popescu, C. C. 2000, *A&AS*, 142, 399

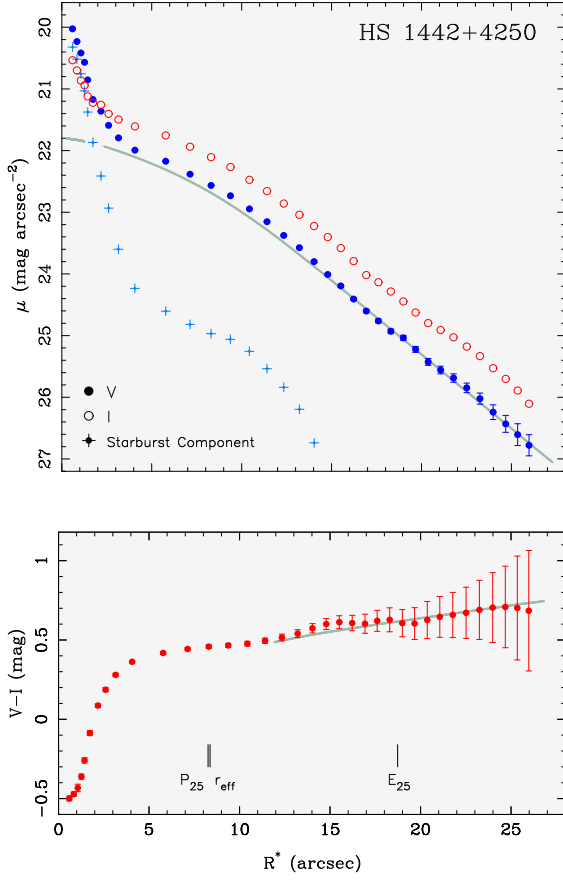


Fig. 4. (a) Surface brightness profiles (SBPs) of HS 1442+4250 in V (filled circles) and I (open circles) derived using the method iii (Papaderos et al. 1996a). The modeled surface brightness distribution of the LSB component in V assuming a modified exponential distribution by Papaderos et al. (1996a) is shown by the thick-grey curve. This model implies a central surface brightness for the LSB component ≈ 1.3 mag fainter than the value predicted by extrapolation of the outer exponential slope of the SBPs to $R^* = 0''$. The surface brightness distribution of the light in excess of the LSB component (crosses) is due to the emission of star-forming regions arranged along the major axis of the galaxy (starburst component) (see Figs. 2 and 3). (b) $(V-I)$ colour profile of HS 1442+4250 computed by subtraction of the SBPs displayed in the upper panel. The thick-grey curve shows the $(V-I)$ colour distribution obtained by subtracting the adopted models of the LSB component intensity distribution in V and I . Both profiles suggest a slow colour increase of 0.3 mag kpc^{-1} with radius and a mean $(V-I)$ colour of $0.63 \pm 0.05 \text{ mag}$ for $R^* \geq 15''$. The effective radius r_{eff} of the V SBP and the isophotal radii P_{25} and E_{25} of the starburst and LSB components at $25 \text{ V mag arcsec}^{-2}$ are indicated.

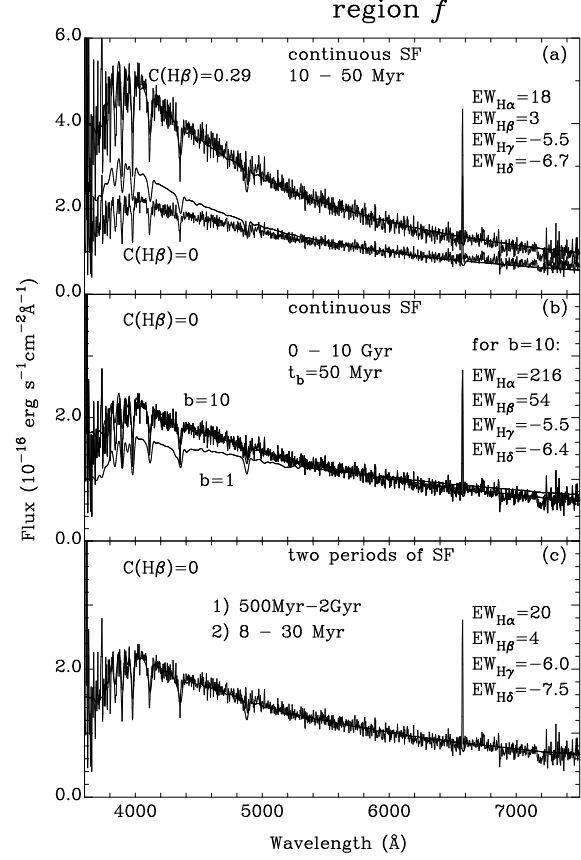


Fig. 7. Spectrum of region f (a) – (c) on which synthetic SEDs are superposed. They are calculated for stellar populations formed continuously within different time intervals. The predicted equivalent widths of hydrogen emission and absorption lines are shown for each model. (a) Synthetic SED corresponds to a stellar population formed continuously between 10 and 50 Myr ago with a constant SFR. The lower SED is superposed on the spectrum uncorrected for extinction and the upper SED is superposed on the spectrum corrected for extinction with $C(\text{H}\beta) = 0.29$. (b) Synthetic SED labeled $b \equiv \text{SFR}(t \leq t_b)/\text{SFR}(t > t_b) = 1$ with $t_b = 50 \text{ Myr}$, corresponding to a stellar population formed continuously between 0 and 10 Gyr with a constant SFR. The synthetic spectrum labeled $b = 10$ corresponds to a stellar population formed continuously between 0 and 10 Gyr with a SFR enhanced by 10 times during $t \leq t_b$. (c) Synthetic SED, calculated for star formation with a constant SFR occurring in two periods: 1) 500 Myr – 2 Gyr ago and 2) 8 – 30 Myr ago. The extinction coefficient is $C(\text{H}\beta) = 0$ for (b) and (c).